Journal of Materials Chemistry C

Ferroelectric Low-Voltage ON/OFF Switching of Chiral Benzene-1,3,5-tricarboxamide Derivative

Journal:	*Journal of Materials Chemistry C*
Manuscript ID	TC-ART-05-2020-002414.R1
Article Type:	Paper
Date Submitted by the Author:	21-Jun-2020
Complete List of Authors:	Wu, Jian-Yun; Tohoku University Takeda, Takashi; Tohoku University Hoshino, Norihisa; Tohoku University, Institute of Multidisciplinary Research for Advanced Materials Akutagawa, Tomoyuki; Tohoku University

ARTICLE

Ferroelectric Low-Voltage ON/OFF Switching of Chiral Benzene-1,3,5-tricarboxamide Derivative

Received 00th January 20xx,
Accepted 00th January 20xx

DOI: 10.1039/x0xx00000x

Jianyun Wu,[a] Takashi Takeda,[a, b]* Norihisa Hoshino,[a, b] and Tomoyuki Akutagawa[a, b]*

The phase transition behaviour, molecular assemblies, and dielectric responses of an *N,N′,N″*-trialkylbenzene-1,3,5-tricarboxamide derivative bearing chiral (*S*)-3,7-dimethyloctyl chains (***S*-3BC**) were compared with those of an *N,N′,N″*-trioctadecylbenzene-1,3,5-tricarboxamide derivative (**3BC**) bearing achiral $–CONHC_{14}H_{29}$ chains. Chiral ***S*-3BC** showed a similar phase transition behaviour to that of achiral **3BC**, and ferroelectric polarization–electric field (*P*–*E*) hysteresis curves were observed in the discotic hexagonal columnar (Col_h) liquid crystal phase. Interestingly, the magnitude of P_r and E_t values of ***S*-3BC** were 5.5-times larger and 13-times smaller than those of **3BC** because of the introduction of the chiral alkyl chains, indicating a useful method to obtain low voltage ON/OFF ratios for the switching device. Much stronger N–H•••O= hydrogen-bonding interactions were observed in ***S*-3BC** than in **3BC** because of much shorter π-stacking distance and blue-shift of the intermolecular asymmetrical N–H vibrational band in the former, which effectively decreased the potential energy barrier for the dipole inversion between N–H•••O= and =O•••H–N orientations and the E_t value.

Introduction

Non-volatile ferroelectric memories are used in information-based technology such as contactless smart cards.[1] Two kinds of ferroelectric mechanisms of the order–disorder and atomic-displacement-types have been recognized in new ferroelectric materials, and the latter has a much faster switching speed than the former.[2] Among the various inorganic ferroelectrics, lead zirconate titanate (PZT) and barium titanate ($BaTiO_3$) are widely used as the atomic-displacement-type ferroelectric memory devices.[1, 3] However, the toxicity, scarce resources, and high costs of the components prevent the development of environmentally friendly memory devices. Thus, chemically modifiable organic ferroelectrics have attracted much attention as a means to control the ferroelectric properties and to fabricate new kinds of low-cost flexible memory devices.[4,5] Dipole inversion and ferroelectricity can be achieved by a range of mechanisms via the design of organic materials; for example, proton transfer in hydrogen bonds, molecular rotation in single crystals or plastic crystals, and atomic displacements in three-dimensional (3D) organic–inorganic hybrid perovskite have recently been exploited.[6–13] In addition, lower-order molecular assemblies such as liquid crystalline phases have been utilized for the formation of ferroelectric materials.[14–16] The chiral smectic C (SmC*) phase of rod-like chiral molecules and banana-shaped molecules show ferroelectric responses on dipole inversion by the application of an external electric field.[17–20] Furthermore, only layer periodicity is observed in the SmC phase, where the molecular long-axis is tilted with respect to the layer, and the crystallinity is much lower than that of the plastic crystals. Therefore, thermally activated molecular motion in liquid crystals is easily activated and designable, unlike those in single crystals and plastic crystals.[21–23]

In addition to liquid crystalline chiral SmC* compounds, other interesting liquid crystalline ferroelectrics have been reported in simple benzene derivatives of an *N,N′,N″*-trialkylbenzene-1,3,5-tricarboxamide derivative (**3BC**), which forms one-dimensional (1D) N–H•••O= hydrogen-bonding molecular assemblies and a discotic hexagonal columnar (Col_h) liquid crystal phase.[24–26] The application of alternating current (AC) voltages in the Col_h phase changes the direction of the dipole moment in the amide-type infinite $(N–H•••O=)_\infty$ hydrogen-bonded chains, resulting in a hysteresis loop in the polarization–electric field (*P*–*E*) curve.[27–31] In liquid crystalline **3BC**, the thermally activated rotations of hydrogen bonds and the melting of the alkyl chains play an essential role in achieving dipole inversion in the 1D column. To obtain the multi-functional ferroelectrics, we also designed a pyrene derivative bearing four tetradecylamide ($–CONHC_{14}H_{29}$) chains, which showed the Col_h liquid crystal phase, organogel and nanowire formation, concentration-dependent excimer emission, current-switching, and ferroelectricity.[32–34] In particular, the molecular design of the π-molecular core enables thermal-tolerant ferroelectrics based on tetrabenzo-porphyrin derivative bearing four $–CONHC_{14}H_{29}$ chains, which showed a ferroelectric *P*–*E* hysteresis curve at 503 K.[35] Therefore, the design of π-electronic systems is a useful approach to design multi-functional molecular materials with specific optical, electrical, and magnetic properties. Furthermore, the non-π-

[a] *Graduate School of Engineering, Tohoku University, Sendai 980-8579, Japan.*
[b] *Institute of Multidisciplinary Research for Advanced Materials (IMRAM), Tohoku University, 2-1-1 Katahira, Aoba-ku, Sendai 980-8577, Japan. E-mail: akutagawa@tohoku.ac.jp*

† Footnotes relating to the title and/or authors should appear here.
Electronic Supplementary Information (ESI) available: [details of any supplementary information available should be included here]. See DOI: 10.1039/x0xx00000x

planar electronic system of 1,12-dimethylbenzo[*c*]phenanthrene (dimethylhelicene) derivatives bearing two $–CONHC_{14}H_{29}$ chains has been shown to form a ferroelectric two-dimensional (2D) lamella-type mesophase, in which the ferroelectric parameters of remanent polarization (P_r) and coercive electric field (E_t) were much larger than those of the 1D columnar Col_h phase.[36] However, the large E_t-value of 22 V μm^{-1} in the 2D hydrogen-bonding layer increases the switching voltage for dipole inversion and is unfavorable for memory device applications. To decrease the E_t-value and increase the P_r-value, further chemical design is needed to achieve high-performance switching memory device under a low-voltage supply.

The introduction of chiral alkyl chains into a rod-like molecule can yield a ferroelectric chiral SmC* phase. Chiral *S*- or *R*-molecules form the polar molecular assembly structures, and an equimolar mixture becomes a non-polar molecular assembly. We have already reported the structure of the molecular assemblies and physical properties of a dimethylhelicene derivative bearing two $–CONHC_{14}H_{29}$ chains, for which ferroelectricity is only observed in the racemic derivative.[35] Liquid crystal formation and the ferroelectric response were not observed in chiral *S*- and *R*-helicene derivatives. The polar chiral structural unit contributes to the macroscopic dipole moment together with the polarization of N–H•••O= amide unit. However, the ferroelectricity of the racemic dimethylhelicene derivative is controlled by the presence of the polar amide unit alone.

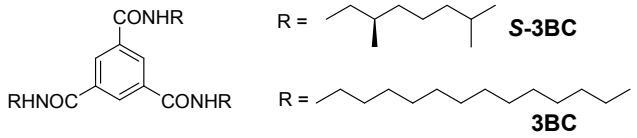

Scheme 1. Molecular structures of chiral ***S*-3BC** and achiral **3BC**.

To control the P_r- and E_t-values in Col_h liquid crystal phase, we focused on chiral **3BC** derivative (***S*-3BC**), which bears three chiral (*S*)-3,7-dimethyloctyl ($(S)\text{-}C_2H_2C^*H(CH_3)(CH_2)_3CH(CH_3)_2$) chains,[37,38] and the phase transition behaviour, liquid crystal formation, molecular assemblies, and ferroelectric response were compared with those of achiral **3BC**, which bears three $–CONHC_{14}H_{29}$ chains (Scheme 1). The mixing states and majority rule between **3BC** and ***S*-3BC** at the molecular level in the solution phase have been extensively discussed.[37–40] However, the dielectric response and ferroelectric behaviour of ***S*-3BC** have not been examined. In this study, we identified the low-switching voltage ferroelectric response of ***S*-3BC**, which can be explained by the formation of much stronger hydrogen-bonding interaction in the 1D π-stacking column than that of **3BC**.

Results and discussion

Chiral ***S*-3BC** was synthesized from the corresponding homochiral (*S*)-3,7-dimethyloctylamine and benzene tricarbonylchloride,[37,38] yielding a white powder. The TG curves of ***S*-3BC** and **3BC** reveal almost the same thermal decomposition behaviours at 520 K after the phase transition to an isotropic liquid (IL) (Fig. S1). The DSC curves of ***S*-3BC** and **3BC** indicate similar two-steps solid–mesophase (S–M) and M–IL phase transitions (Fig. 1a). The reversible S–M and M–IL phase transition temperatures of chiral ***S*-3BC** were observed at 392 and 505 K, respectively, which are 54 and 22 K higher than those of **3BC** at 338 and 483 K. The transition enthalpy change (ΔH, kJ mol^{-1}) of the S–M and M–IL phase transitions of ***S*-3BC** were 19.4 and 29.6 kJ mol^{-1}, respectively. Although the ΔH value of the S–M phase transitions for ***S*-3BC** and **3BC** were almost the same as each other, the ΔH value of the M–IL phase transition for ***S*-3BC** was 24.2 kJ mol^{-1} larger than that of **3BC**. The N–H•••O= hydrogen-bonding interaction of ***S*-3BC** is larger than that of **3BC**. Figs. 1b and 1c show the polarizing optical microscopy (POM) images of ***S*-3BC** under a crossed-Nicol optical arrangement at 375 K (S phase) and 425 K (M phase), respectively. There was no fluidic behaviour in the S phase at 375 K, whereas both fluidic and birefringence behaviours with a characteristic texture of the liquid crystalline phase were observed at 425 K. The M phase of **3BC** has been characterized as a discotic hexagonal columnar (Col_h) liquid crystal phase, and a similar Col_h phase has been observed in M phase of ***S*-3BC**. Although the numbers of carbon atoms in the lateral alkyl chains for ***S*-3BC** and **3BC** differ, the magnitude of the intermolecular interactions in the Col_h phase of ***S*-3BC** was larger than that of the Col_h phase of **3BC** because of the much higher M–IL phase transition temperature.

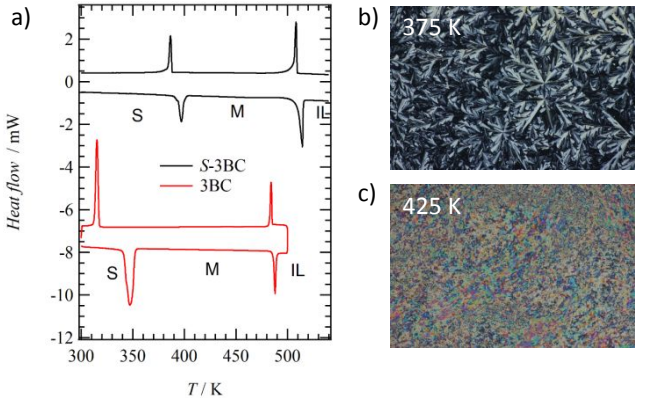

Fig. 1. Phase transition behaviours of chiral ***S*-3BC** and achiral **3BC**. a) DSC diagrams of ***S*-3BC** (black) and **3BC** (red). The S, M, and IL correspond to the solid, Col_h liquid crystal, and isotropic liquid phases, respectively. POM images of ***S*-3BC** under a crossed-Nicole optical arrangement of b) S phase at 375 K and c) Col_h liquid crystal phase at 425 K.

The difference in the thermal properties for ***S*-3BC** and **3BC** is mainly dominated by the amide-type intermolecular N–H•••O= hydrogen-bonding interaction in the Col_h liquid crystal phase. In the solid-state IR spectra, a free N–H asymmetrical stretching vibrational band ($\nu_{N\text{-}H}$) at 3400–3500 cm^{-1} was observed at a much larger energy than that of the intermolecular hydrogen-bonding $\nu_{N\text{-}H}$ band at 3060–3330 cm^{-1}.[41,42] Typical $\nu_{N\text{-}H}$ bands of ***S*-3BC** were observed at 3230 and 3074 cm^{-1}, whereas those of **3BC** were observed at 3238 and 3080 cm^{-1} (Fig. S2). The intermolecular hydrogen-bonding $\nu_{N\text{-}H}$ band was about 150 cm^{-1} red-shifted from that of the free $\nu_{N\text{-}H}$ band, suggesting the effective formation of intermolecular amide-type N–H•••O= hydrogen-bonding interactions both in

***S*-3BC** and **3BC**. Interestingly, the $\nu_{N\text{-}H}$ bands of ***S*-3BC** were slight blue-shifted (6–8 cm^{-1}) in contrast with those of **3BC**, suggesting stronger hydrogen-bonding interactions in ***S*-3BC** than in **3BC** in the solid state.

The formation of a hydrogen-bonded 1D molecular assembly of ***S*-3BC** was confirmed by the formation of organogels, nanofibers, and lyotropic liquid crystalline phases. Figs. 2 show the photographs of organogels and scanning electron microscopy (SEM) images of nanofibers on the highly oriented pyrolytic graphite (HOPG) substrate surface. Transparent organogels of ***S*-3BC** were observed in dimethylsulfoxide (DMSO) and CH_3CN with a fixed concentration of 20 mM, whereas a white opaque organogel was observed in acetone (Table S1). Highly viscous transparent liquids of ***S*-3BC** were observed in cyclohexane, benzene, toluene, and $CHCl_3$, and the solvent-dependent gelling behaviours were associated with the solubility of ***S*-3BC** in these solvents. The formation of organogels of ***S*-3BC** is consistent with the existence of 1D hydrogen-bonded molecular assemblies. Fig. 2b show the 3D network of 1D fibrous molecular assemblies in the xerogel state of ***S*-3BC** on a HOPG substrate (Fig. S4). Each nanofiber was entangled with each other, forming 3D nanopores to capture the solvent molecules in an organogel state. The expanded SEM images of one nanofiber are suggestive of a high-order helical molecular assembly (Figs. 2c and 2d). The clockwise helical 1D assemblies with diameters ranging from 100 to 1000 nm are consistent with the formation of the long-range 1D chiral N–H•••O= hydrogen-bonding molecular assemblies of ***S*-3BC**.

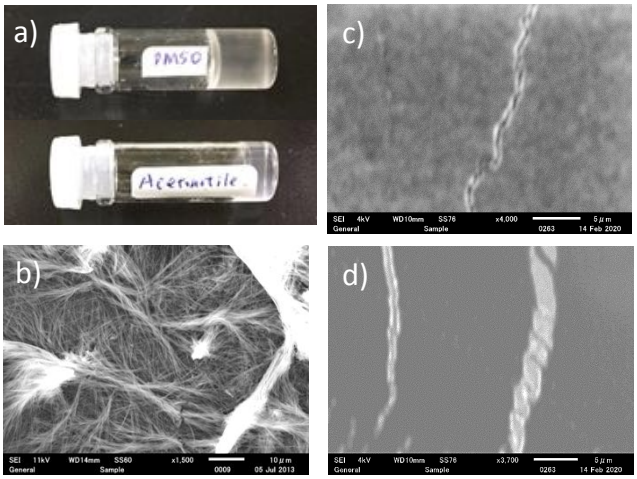

Fig. 2. Molecular assemblies of ***S*-3BC**. a) Organogels in DMSO (top) and CH_3CN (bottom) with a concentration of 5 mM. SEM images of b) xerogels and nanofiber network on HOPG. The scale bar indicates 10 μm. c, d) SEM images of one helical nanofiber with clockwise helicity on HOPG with a scale-bar of 5 μm.

Fig. 3 summarizes the structures of the molecular assemblies of ***S*-3BC** based on the X-ray diffraction experiments. The high crystallinity of ***S*-3BC** at 290 K was confirmed by the sharp Bragg reflections at all measured 2θ angles. The diffraction pattern of ***S*-3BC** at 410 K became quite simple and is characteristic of the formation of Col_h liquid crystal phase[42, 43] and is similar to that of **3BC** at 400 K. The diffraction peaks at 2θ = 5.10°, 8.90°, and 10.28° of ***S*-3BC** at 410 K correspond to *d*-spacings of 1.73, 0.995, and 0.861 nm, respectively, which were indexed to the 100, 110, and 200 diffraction peaks of the hexagonal lattice of Col_h phase. The maximum length of 2.8 nm of the ***S*-3BC** molecule assuming the all-*trans* conformation for the three alkyl chains was about 1 nm longer than d_{100} = 1.73 nm (Fig. 2b), suggesting an interdigitated structure of the three chiral alkyl chains. In contrast, the broad diffuse peaks around 2θ = 18° and 25.5° are assigned to the melting state of alkyl chains and an average π-stacking distance of d_{001} = 0.349 nm. In contrast, the diffraction peaks corresponding to d_{100}, d_{110}, and d_{001} for **3BC** were observed at 2θ = 3.94°, 7.32°, and 22.7 °, indicating periodicities of 2.240, 1.208, and 1.045 nm, respectively, and the melting state of alkyl chains and an average π-stacking distance were observed at 2θ = 19.0° and 22.7° with d_{001} = 0.392 nm. Interestingly, the average columnar distance (d_{001} = 0.349 nm) in the hexagonal arrangement in the Col_h liquid crystal phase of ***S*-3BC** was 0.043 nm shorter than that of **3BC** with d_{001} = 0.392 nm, which effectively decreased the π-stacking distance in the columnar assembly and increased the strength of N–H•••O= hydrogen-bonding interaction along the π-stacking column. This result is consistent with the formation of densely packed molecular assemblies in the branched-alkyl-chain compounds unlike those of the elongated normal chain analogs.[44] The much smaller molecular size and stronger hydrogen-bonding interaction of ***S*-3BC** affect the potential energy curve for the dipole inversion of the N–H•••O= unit and the ferroelectric parameters P_r- and E_t-values.

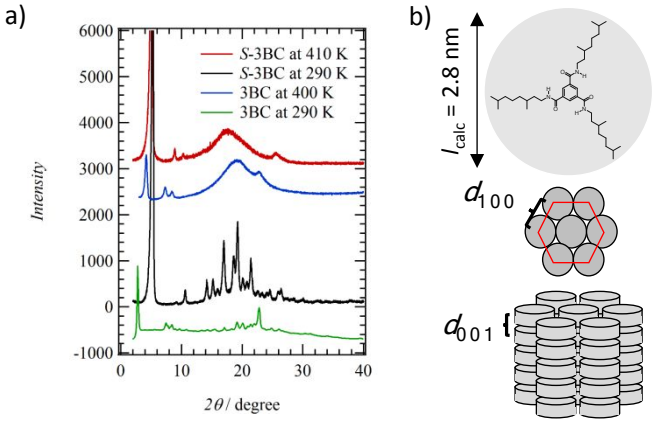

Fig. 3. Molecular assemblies of ***S*-3BC**. a) Temperature-dependent XRD patterns of ***S*-3BC** at 290 K (S phase) and 410 K (M phase) together with Col_h liquid crystal phase of **3BC** at 290 K (S phase) and400 K (M phase). b) Schematic model of the Col_h phase showing the intercolumn and intracolumn *d*-spacings (d_{100} and d_{001}, respectively). The ideal maximum length (l_{calc}) of ***S*-3BC** is about 2.8 nm, assuming the all-*trans* conformation of three chiral alkyl-chains.

The temperature (*T*) and frequency (*f*) dependent dielectric constants are responsible for the motion freedom of the polar structural unit in the molecular assembly.[45] For instance, the inversion of the polar hydrogen-bonding N–H•••O= amide unit and the thermally activated motional freedom of the chiral alkyl chains in Col_h liquid crystal phase can be detected by dielectric measurements. When the motional frequency of the polar structural unit is consistent with the measured *f*-values, large dielectric responses are observed in the both the real (ε_1) and imaginary (ε_2) parts depending on the magnitude of the *f*-values (Fig. S8). Figs. 4a and 4b show the *T*- and *f*-dependent ε_1-

responses of ***S*-3BC**. The overall ε_1-response including both S–Col$_h$ and Col$_h$–IL phase transitions showed huge ε_1 enhancements on increasing in both the *T* and *f*, and the maximum ε_1-value at 524 K with *f* = 100 Hz reached ε_1 = 3000 for the Col$_h$–IL phase transition temperature (Fig. 4a). The ε_1-peaks were observed at the Col–IL phase transition temperature at *f* = 1–10 kHz, which corresponds to the ferroelectric–paraelectric phase transition (see the section concerning *P*–*E* hysteresis). The chiral alkyl chains in Col$_h$ liquid crystal phase were thermally melted with the dipole fluctuation, which drastically enhanced the ε_1 values at low *f*.

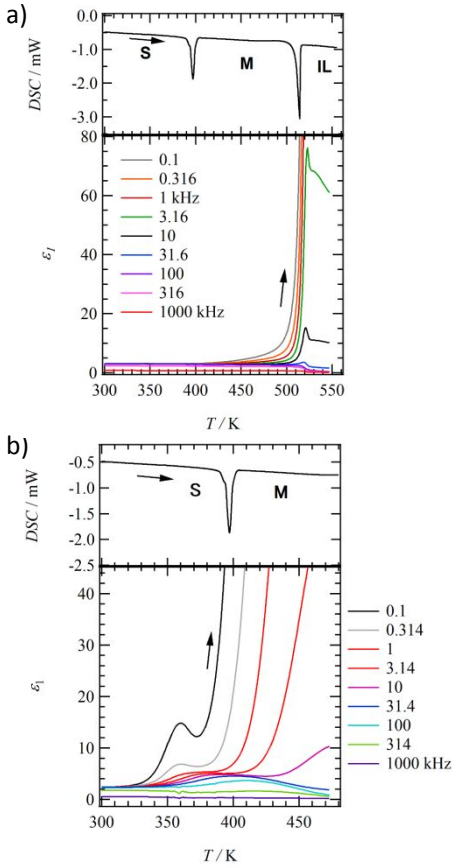

Fig. 4. *T*- and *f*-dependent real part (ε_1) of the dielectric constants of chiral ***S*-3BC**. a) Overall ε_1-response around the Col$_h$–IL phase transition and b) Debye-type ε_1-anomaly around S–Col$_h$ phase transition at 392 K together with the DSC curves of the heating process.

The thermally activated motional freedom of chiral alkyl chains was confirmed by the *T*- and *f*- dependent ε_1-responses around S–Col$_h$ phase transition temperature (Fig. 4b). The dielectric ε_1-peak (T_{p1}) at *f* = 100 Hz and *T* = 361 K was shifted to the much higher T_{p1}-values on increasing the measurement *f*-values. This *f*–T_{p1} response has been observed in a Debye-type relaxation process of the polar structural unit at S–Col$_h$ phase transition. The thermally activated melting state of chiral alkyl chains was observed in the dielectric relaxation process. The ln (τ)–T_{p1}^{-1} plots of ***S*-3BC** clearly indicate a linear correlation (Fig. S9), where the τ-value is the relaxation time of the inverse of the measured *f*-values of the $\tau = 1/(2\pi f)$, indicating an activation energy of E_a =1.567 eV for the thermally activated motional freedom of the chiral alkyl chains. The melted chiral alkyl chains in Col$_h$ liquid crystal phase drastically enhanced the total ε_1-values because of the large amplitude of motional freedom for dipole structural unit.

To confirm the ferroelectric response of ***S*-3BC**, the *T*- and *f*-dependent *P*–*E* hysteresis curves were measured and compared with those of the ferroelectric **3BC** (Fig. S11). Fig. 5a shows the typical ferroelectric *P*–*E* hysteresis curves of the Col$_h$ phase of **3BC** at *T* = 348 K with *f* = 0.2 Hz (black curve) and *f* = 0.5 Hz (red curve). Large P_r-values were observed at low *f*, which is consistent with the existence of slow and collective dipole inversion process in the polar N–H•••O= hydrogen-bonding chains on the application of an external electric field along the π-stacking axis. Typical P_r- and E_c-values of the Col$_h$ phase of **3BC** at 348 K were observed at 0.8 μC cm^{-2} and 22 μVcm^{-1}, respectively. The same ferroelectric *P* – *E* hysteresis behaviour in Col$_h$ liquid crystal phase at *T* = 393 K was observed in ***S*-3BC** at *f* = 0.5 Hz (Fig. 5b). In contrast, the linear *P* – *E* behaviours were observed in the S phase at *T* = 273 and 353 K. Therefore, a ferroelectric phase existed in Col$_h$ liquid crystal phase of ***S*-3BC**, similar to that of **3BC**. The chiral alkyl chains of ***S*-3BC** did not disturb the collective inversion of the intermolecular N–H•••O= hydrogen-bonding interactions along the π-stacked columns.

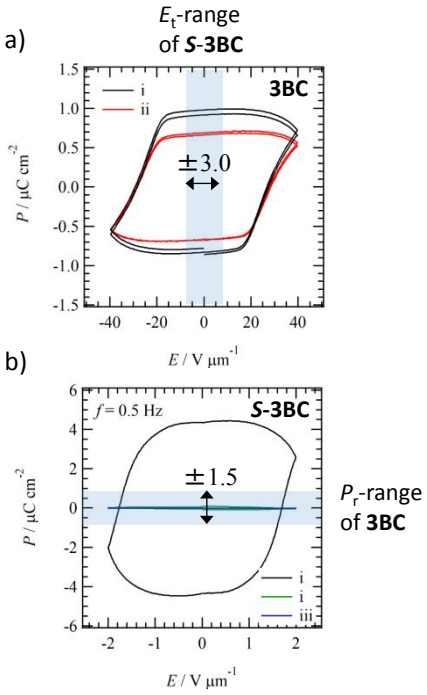

Fig. 5. Ferroelectric *P*–*E* hysteresis curves of the Col$_h$ liquid crystal for **3BC** and ***S*-3BC**. a) The *f*-dependent *P*–*E* curves of **3BC** at *f* = 0.2 Hz (i. black) and *f* = 0.5 Hz (ii. red) and *T* = 348 K (Col$_h$ liquid crystal phase). b) *T*-dependent *P*–*E* curves of ***S*-3BC** at *f* = 0.5 Hz and *T* = 393 K (i. Col$_h$ liquid crystal phase), *T* = 373 K (ii. S phase), and *T* = 353 K (iii. S phase). The vertical and horizontal light-blue areas correspond to the E_t-range of ***S*-3BC** and P_r-range of **3BC**, respectively.

Interestingly, the ferroelectric parameters of P_r- and V_t-values for ***S*-3BC** were drastically different to those of **3BC**. Figs. 5a and 5b show the *P*–*E* hysteresis of **3BC** and ***S*-3BC**, respectively, where the vertical and horizontal light-blue areas correspond to the E_t–range of ***S*-3BC** and P_r–range of **3BC**. The P_r- and E_t-values of the Col$_h$ liquid crystal phase for ***S*-3BC** at 393 K with *f* = 0.5 Hz were observed at 4.5 μC cm^{-2} and 1.7 V μm^{-1},

respectively. The former P_r-value for ***S*-3BC** is 5.5-times larger than that of **3BC**, whereas the latter E_t-value is 13-times smaller than that of **3BC**. Large P_r- and small E_t-values are useful for achieving high-performance ferroelectric memory devices because this increases the ON/OFF ratio and lowers the switching voltage. Thus, the introduction of chiral alkylamide chains into **3BC** is one of the useful approaches to control the ferroelectric P_r- and E_t-values simultaneously. Recently, chiral organic ferroelectrics such as (*R*)- and (*S*)-quinuclidinol and (*R*)- and (*S*)-(*N*,*N*-dimethyl-3-fluoropyrrolidinium) iodide have been reported.[46, 47] The P_r value of the latter crystal was 10 times lower than that of ***S*-3BC**, whereas the P_r value of the former crystal was comparable to that of ***S*-3BC**. On the contrary, the E_t value of the former one was much large than that of ***S*-3BC**. The ferroelectric response of chiral ***S*-3BC** was quite excellent for the memory application due to large P_r and small E_t values.

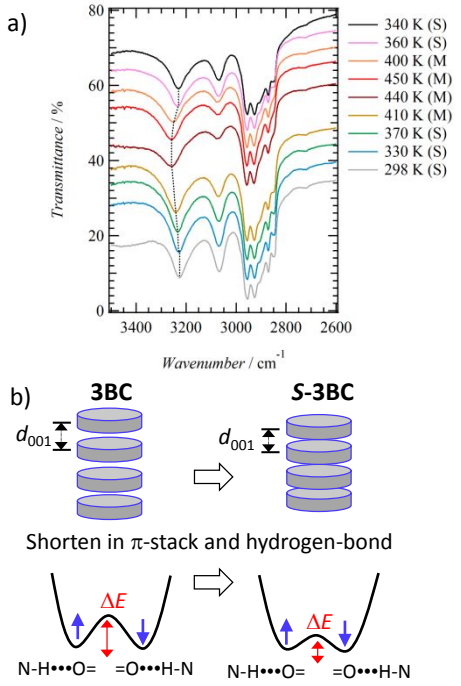

Fig. 6. Role of the intermolecular amide-type N–H•••O= hydrogen-bonding interaction in the Col_h liquid crystal phase on the ferroelectric parameters P_r and E_t. a) *T*-dependent IR spectra of ***S*-3BC** at S and Col_h phases. b) Schematic of the π-stacking column and the double-minimum potential energy curve for the dipole inversion between N–H•••O= and =O•••H–N orientations on the application of E_t. The average π-stacking distance and the N–H•••O= hydrogen-bonding distance of ***S*-3BC** were smaller than those of **3BC**, which reduced the potential energy barrier (ΔE) and resulted in the easy reorientation of hydrogen-bonding amide unit.

The P_r and E_t ferroelectric parameters of chiral ***S*-3BC** and achiral **3BC** were significantly different. Fig. 6 summarizes the *T*-dependent vibrational IR spectra and a schematic model to decrease the E_t-value (Fig. S12). From a structural point of view, the average π-stacking distance of d_{001} = 0.349 nm in the 1D hydrogen-bonding column of ***S*-3BC** was 0.043 nm shorter than that of achiral **3BC** with d_{001} = 0.392 nm, which drastically decreased the N–H•••O= hydrogen-bonding distance in the π-stacking column. The intermolecular hydrogen-bonded $\nu_{N\text{-}H}$ band of ***S*-3BC** in the S phase was observed at 3234 cm^{-1}, whereas that in the Col_h liquid crystal phase indicated a discontinuous shift to 3259 cm^{-1} at S–Col_h phase transition (Fig. 6a). Thermally melted alkylamide chains in the Col_h liquid crystal phase increased the π-stacking and hydrogen-bonding distances simultaneously, which decreased the force constant of N–H•••O= hydrogen-bond resulting in a blue-shift of the $\nu_{N\text{-}H}$ band on increasing the temperature. In contrast, the $\nu_{N\text{-}H}$ bands of the S phase at 330 K and the Col_h liquid crystal phase at 410 K of **3BC** were observed at 3241 and 3252 cm^{-1}, respectively (Fig. S13); the latter $\nu_{N\text{-}H}$ band of the Col_h liquid crystal phase for ***S*-3BC** was observed at 3240 cm^{-1}. Thus, the $\nu_{N\text{-}H}$ band of the Col_h liquid crystal phase of ***S*-3BC** was 12 cm^{-1} lower energy than that of **3BC**, suggesting a stronger N–H•••O= hydrogen-bonding interaction in ***S*-3BC** in the tight 1D π-stacking columns than that of **3BC**.

The dipole inversion between the N–H•••O= and =O•••H–N orientations in the 1D π-stacking column is represented by a symmetrical double-minimum-type potential energy curve (Fig. 6b), where the switching of the two kinds of dipole orientations through the potential energy barrier (ΔE) is activated by the thermal energy or the application of an electric field (k_BT + E_t). When the external E_t voltage has a sufficient magnitude to satisfy the condition of $\Delta E < k_BT + E_t$, a collective dipole inversion occurs in the 1D hydrogen-bonding column. The formation of much stronger hydrogen-bonding interactions decreases the magnitude of ΔE, and much smaller magnitudes of E_t are sufficient to induce dipole inversion. In contrast, the P_r-value is associated with the total dipole moment of chiral ***S*-3BC**, and the theoretical dipole moment of ***S*-3BC** dodecamer has been reported to be μ = 111.0 Debye.[48] We also estimated the theoretical polarization of 4.26 μC cm^{-2}, which is nearly consistent with that of the experimental value of $P_r \approx$ 4.42 μC cm^{-2} (Fig. S11). The P_r-value of **3BC** derivative depends on the carbon number of the lateral –$CONHC_nH_{2n+1}$ chains; for instance, the P_r-values of **3BC** with *n* = 6 and 18 had P_r-values of 2 and 7μC cm^{-2}, respectively.[30] The experimental P_r-value of ***S*-3BC** is roughly consistent with that of **3BC** derivatives according to the linear *n*-dependence.[30-32] The chiral hydrogen-bonded (***S*-3BC**)$_\infty$ columns can easily orient on the ITO electrode with respect to the normal direction of 1D column to the substrate surface. In contrast, the helical 1D columnar assembly of ***S*-3BC** resulted in a drastically decreased inversion energy of the intermolecular hydrogen bonding interaction allowing the appearance of ferroelectricity.

Conclusions

A chiral *N,N′,N″*-trialkylbenzene-1,3,5-tricarboxamide derivative bearing (*S*)-3,7-dimethyloctyl chains (***S*-3BC**) was evaluated in terms of its phase transition, molecular assembly structure, and ferroelectricity. The phase transition behaviour of S–Col_h and Col_h–IL states for ***S*-3BC** was almost the same as that of **3BC** bearing three –$CONHC_{14}H_{29}$ chains, although the thermal phase transition temperature of ***S*-3BC** was higher than that of **3BC**. Chiral ***S*-3BC** formed organogels and helical nanofibers via the formation of densely packed 1D hydrogen-bonding molecular assemblies. The introduction of chiral alkylamide chains into **3BC** did not affect the formation of the

1D hydrogen-bonding columnar Col_h liquid crystal phase, where the strength of N−H•••O= hydrogen-bonding and π-stacking interactions in ***S*-3BC** was larger than those of **3BC**. The P_r-value of ***S*-3BC** was 5.5-times larger than that of **3BC** at T = 348 K, whereas the E_t-value of ***S*-3BC** was 13-times smaller than that of achiral **3BC**. The much larger P_r-value and smaller E_t-value are useful for the design of high-performance non-volatile memory devices based on large ON/OFF ratios and low switching voltages. The formation of strong N−H•••O= hydrogen-bonding interactions decreased the potential energy barrier for the dipole inversion of the hydrogen-bonding units, which effectively suppressed the E_t-value. Chiral hydrogen-bonding organic ferroelectrics are candidate materials for use in excellent non-volatile flexible memory devices.[49]

Conflicts of interest

There are no conflicts to declare.

Acknowledgements

This work was supported by a Grant-in-Aid for Scientific Research on KAKENHI Kibankenkyu (A) (JP19H00886), JST CREST Grant Number JPMJCR18I4, and "Dynamic Alliance for Open Innovation Bridging Human, Environment and Materials" from MEXT.

Notes and references

1 *Nanoelectronics and Information Technology: Advanced Electronic Materials and Novel Devices. 2nd Ed*., R. Waser ed., WILEY VCH, 2003.
2 *Principles and Applications of Ferroelectrics and Related Materials*, M. E. Lines, A. M. Glass, eds., Oxford University Press, New York, 1977.
3 J. F. Scott, *Ferroelectric Memories*, Springer–Verlag, 2000.
4 S. Horiuchi, Y. Tokura, *Nat. Mater*., 2008, **7**, 357–366.
5 T. Hang, W. Zhang, H. –Y. Ye, R.-G. Xiong, *Chem. Soc. Rev*., 2011, **40**, 3577–3598.
6 T. Akutagawa, S. Takeda, T. Hasegawa, T. Nakamura, *J. Am. Chem. Soc*., 2004, **126**, 291–294.
7 S. Horiuchi, Y. Tokunaga, G. Giovannetti, S. Picozzi, H. Itoh, R. Shimano, R. Kumai, Y. Tokura, *Nature*, 2010, *463*, 789–792.
8 T. Akutagawa, H. Koshinaka, D. Sato, S. Takeda, S. Noro, H. Takahasi, R. Kumai, Y. Tokura, T. Nakamura, *Nat. Mater*., 2009, **8**, 342−347.
9 J. Harada, T. Shimojo, H. Oyamaguchi, H. Hasegawa, Y. Takahashi, K. Satomi, Y. Suzuki, J. Kawamata, T. Inabe, *Nat. Chem*., 2016, **8**, 946–952.
10 J. Harada, Y. Kawamura, Y. Takahashi, Y. Uemura, T. Hasegawa, H.; Taniguchi, K. Maruyama, *J. Am. Chem. Soc*., 2019, **141**, 9349–9357.
11 W. –Q. Liao, D. Zhao, Y. –Y., Tang, Y. Zhang, P. –E. Li, P.-P. Shi, X.-G. Chen, Y.-M. You, R. -G. Xiong, *Science*, 2019, **363**, 1206–1210.
12 W. Xu, P. Li, Y. Tang, W. Zhang, R. –G. Xiong, A. A. Chen, *J. Am. Chem. Soc*., 2017, **139**, 6369–6375.
13 H. Morita, R. Tsunashima, S. Nishihara, K. Inoue, Y. Omura, Y. Suzuki, J. Kawamata, N. Hoshino, T. Akutagawa, *Angew. Chem., Int. Ed*., 2019, **58**, 9184–9187.
14 J. P. F. Lagerwall, F. Giesselmann, *ChemPhysChem*., 2006, **7**, 20–45.
15 D. M. Walba, E. Körblova, R. Shao, J. E. Maclennan, D. R. Link, M. A. Glaser, N. A. Clark, *Science*, 2000, **288**, 2181–2184.
16 M. Hird, *Liq. Cryst*., 2011, **38**, 1467–1493.
17 R. P. Lemieux, *Chem. Soc. Rev*., 2007, **36**, 2033–2045.
18 T. Niori, T. Sekine, J. Watanabe, T. Furukawa H. Takezoe, *J. Mater. Chem*., 1996, **6**, 1231–1233.
19 G. Pelzl, S. Diele, W. Weissflog, *Adv. Mater*., 1999, **11**, 707–724.
20 R. A. Reddy, C. Tschierske, *J. Mater. Chem*., 2006, **16**, 907–961
21 A. Tayi, A. Kaeser, M. Matsumoto, T. Aida, S. I. Stupp, *Nat. Chem*., 2015, **8**, 281–294.
22 D. Miyajima, F. Araoka, H. Takezoe, J. Kim, K. Kato, M. Takata, T. Aida, *Science*, 2012, **336**, 209−213.
23 T. Akutagawa, *Mater. Chem. Front*., 2018, **2**, 1064–1073.
24 Y. Matsunaga, N. Miyajima, Y. Nakayasu, S. Sakai, M. Yonenaga, *Bull. Chem. Soc. Jpn*., 1988, **61**, 207–210.
25 Y. Yasuda, E. Iishi, H. Inada, Y. Shirota, *Chem. Lett*., 1996, **25**, 575–576.
26 K. Hanabusa, C. Koto, M. Kimura, H. Shirai, A. Kakehi, *Chem. Lett*., 1997, **26**, 429–430.
27 C. F. C. Fitié, W. S. C. D. Roelofs, M. Kemerink, R. P. Sijbesma, *J. Am. Chem. Soc*., 2010, **132**, 6892–6893.
28 C. F. C. Fitié, W. S. C. Roelofs, P. C. M. M. Magusin, M. Wübbenhorst, M. Kemerink, R. P. Sijbesma, *J. Phys. Chem. B*, 2012, **116**, 3928–3937.
29 Y. Shishido, H. Anetai, T. Takeda, N. Hoshino, S. Noro, T. Nakamura, T. Akutagawa, *J. Phys. Chem. C*., 2014, **118**, 21204–21214.
30 I. Urbanaviciute, X. Meng, T. D. Cornelissen, A. V. Gorbunov, S. Bhattacharjee, R. P. Sijbesma, M. Kemerink, *Adv. Electron. Mater*., 2017, **3**, 1600530–1–7.
31 I. Urbanaviciute, S. Bhattacharjee, M. Biler, J. A. Lugger, T. D. Cornelissen, P. Norman, M. Linares, R. P. Sijbesma, M. Kemerink, *Phys. Chem. Chem. Phys*., 2019, **21**, 2069–2079
32 H. Anetai, Y. Wada, T. Takeda, N. Hoshino, S. Yamamoto, M. Mitsuishi, T. Takenobu, T. Akutagawa, *J. Phys. Chem. Lett*., 2015, **6**, 1813–1818.
33 H. Anetai, T. Takeda, N. Hoshino, Y. Araki, T. Wada, S. Yamamoto, M. Mitsuishi, H. Tsuchida, T. Ogoshi, T. Akutagawa, T. *J. Phys. Chem. C*, 2018, **122**, 6323–6331.
34 H. Anetai, K. Sambe, T. Takeda, N. Hoshino, T. Akutagawa, *Chem. Eur. J*., 2019, **25**, 11233‑11239.
35 J. Wu, T. Takeda, N. Hoshino, Y. Suzuki, J. Kawamata, T. Akutagawa, *J. Phys. Chem. C*., 2019, **123**, 22439–22446.
36 H. Anetai, T. Takeda, N. Hoshino, H. Kobayashi, N. Saito, M. Shigeno, M. Yamaguchi, T. Akutagawa, *J. Am. Chem. Soc*., 2019, **141**, 2391–2397.
37 L. Brunsveld, A. P. H. J. Schenning, M. A. C. Broeren, H. M. Janssen, J. A. J. M. Vekemans, E. W. Meijer, *Chem. Lett*., 2000, **2000**, 292–293.
38 P. J. M. Stals, M. M. J. Smulders, R. Mart-Rapffln, A. R. A. Palmans, E. W. Meijer, *Chem. Eur. J*., 2009, **15**, 2071–2080.
39 A. J. Wilson, M. Masuda, R. P. Sijbesma, E. W. Meijer, *Angew. Chem. Int. Ed*., 2005, **44**, 2275–2279.
40 K. Hanabusa, M. Yamada, M. Kimura, H. Shirai, *Angew. Chem., Int. Ed*., 1996, **35**, 1949–1951.
41 *The Amide Linkage: Structural Significance in Chemistry, Biochemistry, and Materials Science*. C. M. Breneman, J. F. Liebman, eds., Wiley-InterScience, Weinheim, 2000.
42 T. Wöhrle, I. Wurzbach, J. Kirres, A. Kostidou, N. Kapernaum, J. Litterscheidt, C. Haenle, P. Staffeld, A. Baro, F. Giesselmann, S. Laschat, *Chem. Rev*., 2016, **116**, 1139−1241.
43 S. Chandrasekhar, G. S. Ranganath, *Rep. Prog. Phys*., 1990, **53**, 57−84.
44 A. Timme, R. Kress, R. Q. Albuquerque, H. –W. Schmidt, *Chem. Eur. J*., 2012, **18**, 8329–8339.

45 K. C. Kao, *Dielectric Phenomena in Solids*, Elsevier, Amsterdam, 2004.
46 P. –F. Li, W. –Q. Liao, Y. –Y. Tang, W. Qiao, D. Zhao, Y. Ai, Y. –F, Yao, R. –G. Xiong, *Proc. Nat. Acad. Sci. USA*, 2019, **116**, 5878–5885.
47 Y. Ai, D. Wu. M. Yang, P. Wang, W. He, W. Liao, *Chem. Commun*., 2020. 10.1039/d0cc02547j.
48 R. Q. Albuquerque, A. Timme, R. Kress, J. Senker, H. –W. Schmidt, *Chem. Eur. J*., 2013, **19**, 1647−1657.
49 P. –F. Li, Y. –Y. Tang, Z. –X. Wang, H. –Y. Ye, Y. –M. You, R. –G. Xiong, *Nature Commn*., 2016, **7**, 13635–1–9.

TOC Figure

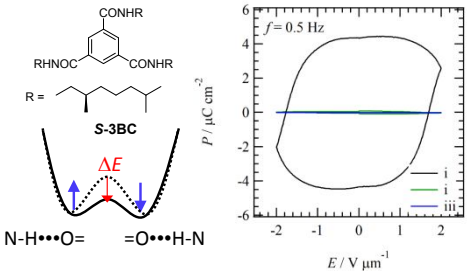

Chiral liquid crystalline benzene trialkylamide derivative showed much lower coercive electric field for ferroelectric switching.